




## Coupled lattice Boltzmann–large eddy simulation model for three-dimensional multiphase flows at large density ratio and high Reynolds number

Xiang An <sup>1</sup>, Bo Dong <sup>1,\*</sup>, Yong Wang,<sup>1</sup> Yajin Zhang <sup>1</sup>, Xun Zhou,<sup>2</sup> and Weizhong Li <sup>1</sup>

<sup>1</sup>Key Laboratory of Ocean Energy Utilization and Energy Conservation of Ministry of Education, School of Energy and Power Engineering, Dalian University of Technology, Dalian 116024, People's Republic of China

<sup>2</sup>Institute of Refrigeration and Air Conditioning Technology, Henan University of Science and Technology, Luoyang 471003, People's Republic of China

 (Received 3 May 2021; revised 23 August 2021; accepted 19 September 2021; published 13 October 2021)

A coupled lattice Boltzmann–large eddy simulation model is developed for modeling three-dimensional multiphase flows at large density ratios and high Reynolds numbers. In the framework of the lattice Boltzmann method, the model is proposed based on the standard Smagorinsky subgrid-scale approach, and a reconstructed multiple-relaxation-time collision operator is adopted. The conservative Allen–Cahn equation and Navier–Stokes equations are solved through the lattice Boltzmann discretization scheme for the interface tracking and velocity field evolution, respectively. Relevant benchmark cases are carried out to validate the performance of this model in simulating multiphase flows at a large density ratio and a high Reynolds number, including a stationary droplet, the process of spinodal decomposition, the Rayleigh–Taylor instability, the phenomenon of a droplet splashing on a thin liquid film, and the liquid jet breakup process. The maximum values of density ratio and Re number are 1000 and 10 240, respectively. The capability and reliability of the proposed model have been demonstrated by the good agreement between simulation results and the analytical solutions or the previously available results.

DOI: [10.1103/PhysRevE.104.045305](https://doi.org/10.1103/PhysRevE.104.045305)

### I. INTRODUCTION

Modeling multiphase flows at large density ratios and high Reynolds numbers has an important guiding significance in many phenomena such as aerospace propulsion systems, food processing, and inkjet printing. A practical and efficient multiphase model under the conditions of large density ratio and high Reynolds number is imperative and helpful for the related industries. In the past decades, the lattice Boltzmann (LB) method has been proved to be a powerful tool in modeling interfacial phenomena in multiphase flows [1,2]. In the LB community, some multiphase LB models have been successively proposed, and they can be divided into four categories: the color-gradient model [3,4], the pseudopotential model [5,6], the free-energy model [7,8], and the phase-field model [9–12]. For the last one, the phase-field theory [13–16] is introduced into the framework of the LB method, in which a single variable known as the order parameter is used to monitor the transition between different phases. The phase-field-based LB method has become one of the most popular numerical simulation methods for dynamic multiphase flows to date [17].

In the phase-field-based LB simulation of dynamic multiphase flows, there is a significant limitation in simulating multiphase turbulent flow at a high Re number, which triggers numerical instability for demanding a low relaxation time. In 1999, He *et al.* [18] proposed an incompressible LB model for simulating multiphase flows, in which they used an

index function to track the interface between different phases. The preliminary version suffered from numerous drawbacks including numerical instability at a large density ratio. This issue was alleviated to a great extent by Lee and Lin [19], and numerical results showed that Lee and Lin's model was capable of simulating multiphase flows at the density ratio of 1000. Unfortunately, Zheng *et al.* [20] pointed out that the two above-mentioned models cannot correctly recover the Cahn–Hilliard equation. This problem was rectified by Zheng *et al.* [20] and Lee and Liu [21] through their modified phase-field-based LB models. In 2013, Zu and He [9] utilized two sets of LB equations to recover the Cahn–Hilliard equation and the divergence-free incompressible Navier–Stokes equations for interface tracking and hydrodynamic properties, and they simulated incompressible binary fluid systems with density and viscosity contrasts. The Rayleigh–Taylor instability was modeled at a Re number of 3000.

Different from the Cahn–Hilliard equation used in the above studies, the Allen–Cahn equation was proposed for interface tracking in Geier *et al.*'s work [22] and Wang *et al.*'s work [23]. Although the equilibrium distribution functions and source terms are different in the above two models, both models are very comparable in terms of accuracy in interface tracking. According to the study of Begmohammadi *et al.* [24], the additional terms in recovering the conservative Allen–Cahn equation in Geier *et al.*'s model can be negligible legitimately, which exactly gives this model an advantage for high-performance computing and nonuniform grids processes. Compared with the Cahn–Hilliard equation, the Allen–Cahn equation contains a lower-order diffusion term. It has been pointed out that the Allen–Cahn-based model

\*Corresponding author: [bodong@dlut.edu.cn](mailto:bodong@dlut.edu.cn)

theoretically has higher numerical accuracy and stability in solving the index parameter than the Cahn-Hilliard-based one [23,25]. Following the above viewpoint, Liang *et al.* [26] proposed a two-dimensional phase-field-based single-relaxation-time (SRT) LB model for large-density-ratio multiphase flows, in which the Allen-Cahn equation is adopted to track the interface, and they simulated the phenomenon of a droplet splashing on a thin liquid film in two dimensions at a Re number of 500. Recently, Zhou *et al.* [27] developed a multiple-relaxation-time (MRT) operator form of the Allen-Cahn-based LB model and investigated the Kelvin-Helmholtz instability and the Rayleigh-Taylor instability in wide ranges of density ratio, viscosity ratio, and Re number. Meanwhile, Zu *et al.* [28] updated their phase-field-based LB model for the binary fluid system by adopting the Allen-Cahn equation for interface tracking, and Liang *et al.* [29] performed the coordinate transformation and proposed an axisymmetric lattice Boltzmann model for multiphase flows. Using the phase-field-based LB model recovering the Allen-Cahn equation, despite simplicity, accuracy, and robustness, the simulation of the multiphase flow at high Re number is still a great challenge due to the numerical instability triggered by the large numerical gradient at the interface and a small relaxation time. Given the application of large eddy simulation (LES) in high-Re number flows, the LES is considered to integrate within the framework of the phase-field-based multiphase LB model.

It has already been demonstrated that LES within the LBM framework not only can accurately describe the turbulence hydrodynamics but also has distinct computational advantages in improving the model robustness and adjusting relevant parameters [30]. Actually, with the increasing popularity of the LB method, the LES has been widely used in single-phase LB models [31–35]. While for multiphase LB models, an efficient coupled LB-LES model capable of simulating multiphase flows at high Re number is still lacking. A few attempts have been made in this regard to date, such as the studies of Banari *et al.* [36,37], where three-dimensional breaking waves were investigated. The phase interface was captured by solving the Cahn-Hilliard advection-diffusion equation, and the LES as a subgrid-scale turbulence model was applied to the velocity field for solving the Navier-Stokes equations. Unfortunately, the third particle distribution function was introduced to solve the Poisson equation for pressure correction iteratively, which led to less efficiency and impaired the inherent simplicity of the LBM, as argued by Lee and Lin [19]. Another is the two-phase LB-LES model developed by Amirshaghghi *et al.* [38]. The Cahn-Hilliard equation and Navier-Stokes equations were filtered by the LES approach. Using the proposed model, they simulated the two-dimensional liquid sheet breakup at different Reynolds numbers ranging 1000–6000. Considering the advantages of the Allen-Cahn equation compared with the Cahn-Hilliard equation in interface tracking as mentioned above, in this work, an efficient three-dimensional multiphase flows model is developed to fill this gap by coupling an Allen-Cahn-based LB model and LES approach.

The proposed model in this work has the following two innovations. First, the three-dimensional MRT collision operator is reconstructed for the Allen-Cahn equation and Navier-Stokes equations, respectively, which has better

accuracy and stability than the SRT operator. Second, the phase-field-based LB model and LES approach are coupled, which indicates the feasibility to simulate the multiphase flows at high Re numbers. The rest of this paper is organized as follows. In Sec. II, the three-dimensional coupled LB-LES model for multiphase flows is introduced systematically. Then the model is verified by several classical numerical examples in Sec. III. Finally, a brief summary is made in Sec. IV.

## II. MATHEMATICAL METHOD

In this section, first, an MRT-LB model for multiphase flows based on phase-field theory is elaborated. Then, an essential introduction to the coupling between the LB model and LES is given.

### A. Three-dimensional MRT LB model for the conservative Allen-Cahn equation

The conservative Allen-Cahn equation can be expressed by [39,40]

$$\frac{\partial \phi}{\partial t} + \nabla \cdot (\phi \mathbf{u}) = \nabla \cdot [M(\nabla \phi - \lambda \mathbf{n})], \quad (1)$$

where  $M$  is the mobility and  $\phi$  is the order parameter used to capture the interface according to phase-field theory. The vectors  $\mathbf{u}$  and  $\mathbf{n}$  are the fluid velocity and the unit value normal to the interface, and the latter is written as

$$\mathbf{n} = \frac{\nabla \phi}{|\nabla \phi|}. \quad (2)$$

$\lambda$  is a function of the order parameter, which is defined by

$$\lambda = \frac{4\phi(1-\phi)}{W}, \quad (3)$$

where  $W$  is the interface thickness.

The MRT-LB evolution equation to solve the conservation Allen-Cahn equation can be written as

$$\begin{aligned} f_i(\mathbf{x} + \mathbf{e}_i \delta_t, t + \delta_t) \\ = f_i(\mathbf{x}, t) - (\mathbf{M}^{-1} \mathbf{S} \mathbf{M})_{ij} [f_j(\mathbf{x}, t) - f_j^{\text{eq}}(\mathbf{x}, t)] + \delta_t F_i, \end{aligned} \quad (4)$$

where  $f_i(\mathbf{x}, t)$  is the particle distribution function for the order parameter, and  $f_i^{\text{eq}}(\mathbf{x}, t)$  is its equilibrium particle distribution function given by

$$f_i^{\text{eq}} = \omega_i \phi \left( 1 + \frac{\mathbf{e}_i \cdot \mathbf{u}}{c_s^2} \right), \quad (5)$$

where  $c_s$  is the sound speed,  $\mathbf{e}_i$  are the discrete velocities, and  $\omega_i$  are the weighting coefficients. In the present study, the D3Q7 lattice model is adopted for solving the conservation Allen-Cahn equation, as shown in Fig. 1.

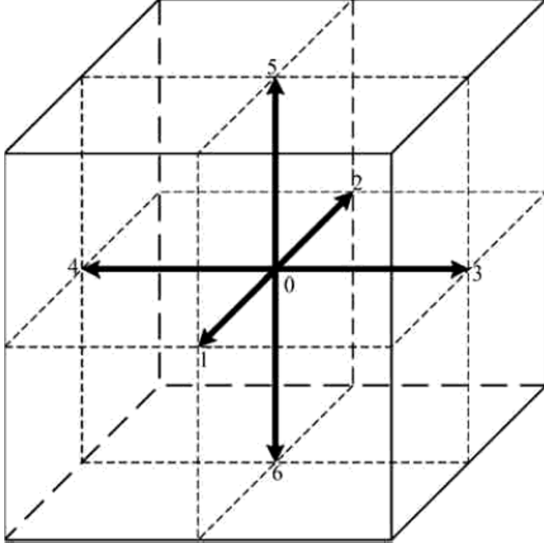


FIG. 1. D3Q7 lattice model.

The corresponding weighting coefficients, sound speed, and discrete velocities are

$$\omega_0 = \frac{1}{4}, \quad \omega_{1-6} = \frac{1}{8}, \quad c_s^2 = \frac{c^2}{4}, \quad (6)$$

$$\mathbf{e}_i = \begin{bmatrix} 0 & 1 & -1 & 0 & 0 & 0 & 0 \\ 0 & 0 & 0 & 1 & -1 & 0 & 0 \\ 0 & 0 & 0 & 0 & 0 & 1 & -1 \end{bmatrix} c, \quad (7)$$

where  $c = \delta_x/\delta_t$  is the lattice speed.

The forcing distribution function  $F_i$  in the LB evolution equation is designed as [41]

$$F_i = \left(1 - \frac{1}{2\tau_f}\right) R_i = \left(1 - \frac{1}{2\tau_f}\right) \frac{\omega_i \mathbf{e}_i \cdot [\partial_t(\phi \mathbf{u}) + c_s^2 \lambda \mathbf{n}]}{c_s^2}. \quad (8)$$

$$\mathbf{R}^m = \mathbf{M} \cdot R_i = [0 \quad \partial_t(\phi u_x) + c_s^2 \lambda n_x \quad \partial_t(\phi u_y) + c_s^2 \lambda n_y \quad \partial_t(\phi u_z) + c_s^2 \lambda n_z \quad 0 \quad 0 \quad 0]^T. \quad (12)$$

Thus the collision process in the moment space is written as

$$\mathbf{m}^* = \mathbf{m} - \mathbf{S}(\mathbf{m} - \mathbf{m}^{\text{eq}}) + \delta_t(\mathbf{I} - 0.5\mathbf{S})\mathbf{R}^m, \quad (13)$$

where  $\mathbf{I}$  is the unit tensor and  $\mathbf{m} = \mathbf{M} \cdot f$ . Besides, the relation between the mobility  $M$  and the relaxation parameter  $\tau_f$  is also derived as

$$M = c_s^2(\tau_f - 0.5)\delta_t, \quad (14)$$

where  $\tau_f = 1/s_1$ . The order parameter  $\phi$ , the density  $\rho$ , and the kinematic viscosity  $\nu$  are determined by

$$\phi = \sum_i f_i, \quad (15)$$

$$\rho = \frac{\phi - \phi_v}{\phi_l - \phi_v}(\rho_l - \rho_v) + \rho_v, \quad (16)$$

Here, the explicit Euler scheme is used to compute the temporal derivative  $\partial_t(\phi \mathbf{u}) = [\phi(t)\mathbf{u}(t) - \phi(t - \delta_t)\mathbf{u}(t - \delta_t)]/\delta_t$ . This term is used in recovering the conservative Allen-Cahn equation; it does not affect the precision of the model although it is a first-order scheme [23,28].  $\tau_f$  is the relaxation time. For the MRT scheme, the diagonal relaxation matrix  $\mathbf{S}$  is given as

$$\mathbf{S} = \text{diag}(s_0, s_1, s_1, s_1, s_2, s_3, s_3). \quad (9)$$

Note that when the parameters  $s_i$  ( $i = 0-3$ ) are equal to each other, the MRT scheme reduces to the SRT scheme. In the D3Q7 lattice model, the transformation matrix  $\mathbf{M}$  is given by [42,43]

$$\mathbf{M} = \begin{bmatrix} 1 & 1 & 1 & 1 & 1 & 1 & 1 \\ 0 & 1 & -1 & 0 & 0 & 0 & 0 \\ 0 & 0 & 0 & 1 & -1 & 0 & 0 \\ 0 & 0 & 0 & 0 & 0 & 1 & -1 \\ 6 & -1 & -1 & -1 & -1 & -1 & -1 \\ 0 & 2 & 2 & -1 & -1 & -1 & -1 \\ 0 & 0 & 0 & 1 & 1 & -1 & -1 \end{bmatrix}. \quad (10)$$

In the execution of the MRT codes, the collision process is implemented in the moment space and the streaming process is executed in velocity space. By premultiplying the transformation matrix, one can derive the equilibrium distribution function in moment space as

$$\mathbf{m}^{\text{eq}} = \mathbf{M} \cdot f^{\text{eq}} = \left[ \phi \quad \phi u_x \quad \phi u_y \quad \phi u_z \quad \frac{3\phi}{4} \quad 0 \quad 0 \right]^T. \quad (11)$$

In the equilibrium distribution function in moment space,  $u_x$ ,  $u_y$ , and  $u_z$  are the components of macroscopic velocity  $\mathbf{u}$ . In the same way; the factor  $R_i$  in forcing distribution function can be presented in moment space as

$$\nu = \frac{\phi - \phi_v}{\phi_l - \phi_v}(\nu_l - \nu_v) + \nu_v. \quad (17)$$

### B. Three-dimensional MRT-LB model for the Navier-Stokes equations

For the incompressible two-phase flows, the fluid velocity  $\mathbf{u}$  in the conservative Allen-Cahn equation is governed by the following Navier-Stokes equations [44]:

$$\nabla \cdot \mathbf{u} = 0, \quad (18)$$

$$\frac{\partial(\rho \mathbf{u})}{\partial t} + \nabla \cdot (\rho \mathbf{u} \mathbf{u}) = -\nabla p + \nabla \cdot [\rho \nu (\nabla \mathbf{u} + \nabla \mathbf{u}^T)] + \mathbf{F}_s + \mathbf{G}, \quad (19)$$

where  $p$  is the hydrodynamic pressure,  $\mathbf{G}$  is the external force, and  $\mathbf{F}_s \mathbf{F}_s$  is the surface tension force, which takes the potential

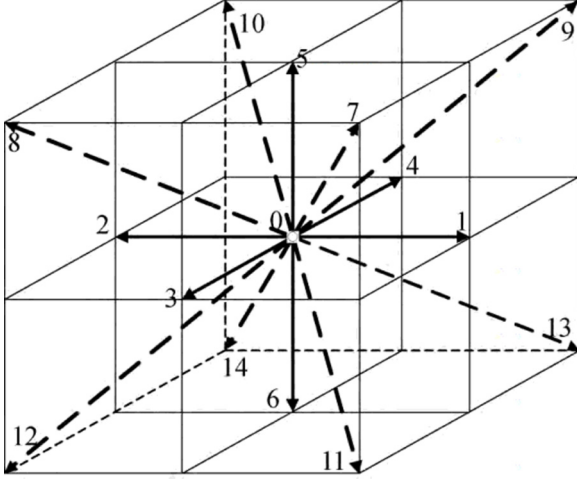


FIG. 2. D3Q15 lattice model.

form of the phase-field model [45],

$$\mathbf{F}_s = \mu \nabla \phi, \quad (20)$$

where  $\mu$  is the chemical potential, and it can be expressed as

$$\mu = 4\beta(\phi - \phi_l)(\phi - \phi_v) \left( \phi - \frac{\phi_l + \phi_v}{2} \right) - k\nabla^2 \phi. \quad (21)$$

In this work,  $\phi_l = 1.0$  and  $\phi_v = 0$  represent the liquid phase and vapor phase, respectively, and the phase interface

is marked by the contour level  $\phi = 0.5$ . Here  $\beta$  and  $k$  are constants related to the interfacial thickness and the surface tension coefficient  $\sigma$  as [23]

$$k = \frac{3W\sigma}{2|\phi_l - \phi_v|^2}, \quad \beta = \frac{12\sigma}{W|\phi_l - \phi_v|^4}. \quad (22)$$

The MRT-LB equation to solve the Navier-Stokes equations reads as

$$\begin{aligned} g_i(\mathbf{x} + \mathbf{e}_i \delta_t, t + \delta_t) \\ = g_i(\mathbf{x}, t) - (\Gamma^{-1} \mathbf{\Lambda} \Gamma)_{ij} [g_j(\mathbf{x}, t) - g_j^{\text{eq}}(\mathbf{x}, t)] + \delta_t G_i, \end{aligned} \quad (23)$$

where  $g_i(\mathbf{x}, t)$  is the particle distribution function, and its equilibrium particle distribution function  $g_i^{\text{eq}}(\mathbf{x}, t)$  is given by

$$g_i^{\text{eq}} = \begin{cases} \frac{\rho}{c_s^2}(\omega_i - 1) + \rho s_i(\mathbf{u}), & i = 0, \\ \frac{\rho}{c_s^2} \omega_i + \rho s_i(\mathbf{u}), & i \neq 0 \end{cases} \quad (24)$$

with

$$s_i(\mathbf{u}) = \omega_i \left[ \frac{\mathbf{e}_i \cdot \mathbf{u}}{c_s^2} + \frac{(\mathbf{e}_i \cdot \mathbf{u})^2}{2c_s^4} - \frac{\mathbf{u} \cdot \mathbf{u}}{2c_s^2} \right]. \quad (25)$$

In the present study, the D3Q15 lattice model is adopted, as displayed in Fig. 2. The corresponding weighting coefficients, sound speed, and discrete velocities are defined as

$$\omega_0 = \frac{2}{9}, \quad \omega_{1-6} = \frac{1}{9}, \quad \omega_{7-14} = \frac{1}{72}, \quad c_s^2 = \frac{c^2}{3}, \quad (26)$$

$$\mathbf{e}_i = \begin{bmatrix} 0 & 1 & -1 & 0 & 0 & 0 & 0 & 1 & -1 & 1 & -1 & 1 & -1 & 1 & -1 \\ 0 & 0 & 0 & 1 & -1 & 0 & 0 & 1 & 1 & -1 & -1 & 1 & 1 & -1 & -1 \\ 0 & 0 & 0 & 0 & 0 & 1 & -1 & 1 & 1 & 1 & 1 & -1 & -1 & -1 & -1 \end{bmatrix} c. \quad (27)$$

The forcing distribution function  $G_i$  in the evolution equation is formulated as

$$G_i = \left( 1 - \frac{1}{2\tau_g} \right) T_i = \left( 1 - \frac{1}{2\tau_g} \right) \omega_i \left( \frac{\mathbf{e}_i \cdot \mathbf{F}}{c_s^2} + \frac{\mathbf{u} \nabla \rho : \mathbf{e}_i \mathbf{e}_i}{c_s^2} \right), \quad (28)$$

where  $\mathbf{F} = \mathbf{F}_s + \mathbf{G}$  is the total force, and  $\tau_g$  is the relaxation time. For the MRT operator, the diagonal relaxation matrix  $\mathbf{\Lambda}$  is adopted:

$$\mathbf{\Lambda} = \text{diag}(s'_0, s'_1, s'_2, s'_3, s'_4, s'_3, s'_4, s'_3, s'_4, s'_5, s'_5, s'_5, s'_5, s'_5, s'_6). \quad (29)$$

In the D3Q15 lattice model, the transformation matrix  $\Gamma$  is given by [46]

$$\Gamma = \begin{bmatrix} 1 & 1 & 1 & 1 & 1 & 1 & 1 & 1 & 1 & 1 & 1 & 1 & 1 & 1 & 1 \\ -2 & -1 & -1 & -1 & -1 & -1 & -1 & 1 & 1 & 1 & 1 & 1 & 1 & 1 & 1 \\ 16 & -4 & -4 & -4 & -4 & -4 & -4 & 1 & 1 & 1 & 1 & 1 & 1 & 1 & 1 \\ 0 & 1 & -1 & 0 & 0 & 0 & 0 & 1 & -1 & 1 & -1 & 1 & -1 & 1 & -1 \\ 0 & -4 & 4 & 0 & 0 & 0 & 0 & 1 & -1 & 1 & -1 & 1 & -1 & 1 & -1 \\ 0 & 0 & 0 & 1 & -1 & 0 & 0 & 1 & 1 & -1 & -1 & 1 & 1 & -1 & -1 \\ 0 & 0 & 0 & -4 & 4 & 0 & 0 & 1 & 1 & -1 & -1 & 1 & 1 & -1 & -1 \\ 0 & 0 & 0 & 0 & 0 & 1 & -1 & 1 & 1 & 1 & 1 & -1 & -1 & -1 & -1 \\ 0 & 0 & 0 & 0 & 0 & -4 & 4 & 1 & 1 & 1 & 1 & -1 & -1 & -1 & -1 \\ 0 & 2 & 2 & -1 & -1 & -1 & -1 & 0 & 0 & 0 & 0 & 0 & 0 & 0 & 0 \\ 0 & 0 & 0 & 1 & 1 & -1 & -1 & 0 & 0 & 0 & 0 & 0 & 0 & 0 & 0 \\ 0 & 0 & 0 & 0 & 0 & 0 & 0 & 1 & -1 & -1 & 1 & 1 & -1 & -1 & 1 \\ 0 & 0 & 0 & 0 & 0 & 0 & 0 & 1 & 1 & -1 & -1 & -1 & -1 & 1 & 1 \\ 0 & 0 & 0 & 0 & 0 & 0 & 0 & 1 & -1 & 1 & -1 & -1 & 1 & -1 & 1 \\ 0 & 0 & 0 & 0 & 0 & 0 & 0 & 1 & -1 & -1 & 1 & -1 & 1 & 1 & -1 \end{bmatrix}. \quad (30)$$

The collision process of the MRT-LB equation for Navier-Stokes equations is also carried out in moment space. After some algebraic manipulations, the equilibrium distribution function  $\mathbf{q}^{\text{eq}}$  and the factor  $\mathbf{T}^m$  in forcing distribution function in the moment space can be derived as

$$\mathbf{q}^{\text{eq}} = \Gamma \cdot g^{\text{eq}} = \left[ 0, 3p + \rho \mathbf{u}^2, -(45p + 5\rho \mathbf{u}^2), \rho u_x, -\frac{7\rho u_x}{3}, \rho u_y, -\frac{7\rho u_y}{3}, \rho u_z, -\frac{7\rho u_z}{3}, \rho(2u_x^2 - u_y^2 - u_z^2), \rho(u_y^2 - u_z^2), \rho u_x u_y, \rho u_y u_z, \rho u_x u_z, 0 \right]^T, \quad (31)$$

$$\mathbf{T}^m = \Gamma \cdot T_i = \left[ (\rho_l - \rho_v) \mathbf{u} \cdot \nabla \phi, -\frac{(\rho_l - \rho_v) \mathbf{u} \cdot \nabla \phi}{3}, -\frac{7(\rho_l - \rho_v) (\mathbf{u} \cdot \nabla \phi)}{3}, F_x, -\frac{7F_x}{3}, F_y, -\frac{7F_y}{3}, F_z, -\frac{7F_z}{3}, \frac{2(\rho_l - \rho_v) \cdot (2u_x \partial_x \phi - u_y \partial_y \phi - u_z \partial_z \phi)}{3}, \frac{2(\rho_l - \rho_v) \cdot (u_y \partial_y \phi - u_z \partial_z \phi)}{3}, \frac{(\rho_l - \rho_v) \cdot (u_x \partial_y \phi + u_y \partial_x \phi)}{3}, \frac{(\rho_l - \rho_v) \cdot (u_y \partial_z \phi + u_z \partial_y \phi)}{3}, \frac{(\rho_l - \rho_v) \cdot (u_x \partial_z \phi + u_z \partial_x \phi)}{3}, 0 \right]^T. \quad (32)$$

The collision process in the moment space reads as

$$\mathbf{q}^* = \mathbf{q} - \mathbf{\Lambda}(\mathbf{q} - \mathbf{q}^{\text{eq}}) + \delta_t(\mathbf{I} - 0.5\mathbf{\Lambda})\mathbf{T}^m, \quad (33)$$

where  $\mathbf{q} = \Gamma \cdot g$  is the particle distribution function in moment space. The relation between the kinematic viscosity  $\nu$  and the relaxation parameter  $\tau_g$  is given by

$$\nu = c_s^2(\tau_g - 0.5)\delta_t, \quad (34)$$

where  $\tau_g = 1/s'_g$ . Note that in the simulations, the relaxation parameter  $s'_g$  is less than 1.0 to avoid divergence. The values of other relaxation parameters in  $\mathbf{S}$  and  $\mathbf{\Lambda}$  are set between 0 and 2. The macroscopic quantities such as velocity  $\mathbf{u}$  and pressure  $p$  are determined by

$$\rho \mathbf{u} = \sum_i \mathbf{e}_i g_i + 0.5\delta_t \mathbf{F}, \quad (35)$$

$$p = \frac{c_s^2}{(1 - \omega_0)} \left[ \sum_{i \neq 0} g_i + 0.5\delta_t (\rho_l - \rho_v) \mathbf{u} \cdot \nabla \phi + \rho s_0(\mathbf{u}) \right]. \quad (36)$$

The gradient term and the Laplace operator are calculated via the second-order isotropic central scheme and are expressed as

$$\nabla \phi(\mathbf{x}) = \sum_{i \neq 0} \frac{\omega_i \mathbf{e}_i \phi(\mathbf{x} + \mathbf{e}_i \delta_t)}{c_s^2 \delta_t}, \quad (37)$$

$$\nabla^2 \phi(\mathbf{x}) = \sum_{i \neq 0} \frac{2\omega_i [\phi(\mathbf{x} + \mathbf{e}_i \delta_t) - \phi(\mathbf{x})]}{c_s^2 \delta_t^2}. \quad (38)$$

It should be noted that the difference scheme not only can preserve a second-order accuracy in space but also can ensure the global mass conservation of a multiphase system [47].

### C. Large eddy simulation

Numerical studies have shown that the applications of the LB method for high Reynolds number flows, without modeling unresolved small-scale effects on large-scale dynamics, result in numerical instability [48]. This is essential because a high Re number requires a relaxation time close to 0.5. In this work, the LES is combined with the LB model to capture the

turbulent scale. The main idea behind the LES is to resolve the large-scale eddies and mimic the presence of small-scale structures via the modeling of subgrid scales [38]. Using the LES approach, a filtering operation is applied to the above phase-field-based LB model and it is defined as

$$\bar{\Phi}(\mathbf{x}) = \int \Phi(\mathbf{x})G(\mathbf{x}, \mathbf{x}')d\mathbf{x}', \quad (39)$$

where  $\Phi$  represents the physical quantity under consideration and  $G$  is the filter function, which is given by

$$G_i(x_i, x'_i) = \begin{cases} 1/\Delta_i, & |x_i - x'_i| \leq \Delta_i/2 \\ 0, & |x_i - x'_i| > \Delta_i/2 \end{cases} \quad (40)$$

with  $\Delta_i$  being the filter width in the direction  $i$ .

Note that the filtering operation is not directly applied to the calculation of the density and kinematic viscosity, and both of them are obtained from the filtered value of the order parameter,

$$\rho = \frac{\bar{\phi} - \phi_v}{\phi_l - \phi_v}(\rho_l - \rho_v) + \rho_v, \quad (41)$$

$$\nu = \frac{\bar{\phi} - \phi_v}{\phi_l - \phi_v}(\nu_l - \nu_v) + \nu_v. \quad (42)$$

### 1. Filtered conservative Allen-Cahn equation and Navier-Stokes equations

When the filtering operation is applied to Eq. (1), it can be written as

$$\frac{\partial \bar{\phi}}{\partial t} + \bar{\nabla} \cdot (\bar{\phi} \bar{\mathbf{u}}) = \bar{\nabla} \cdot [M(\bar{\nabla} \bar{\phi} - \lambda \bar{\mathbf{n}})]. \quad (43)$$

Considering the incompressibility hypothesis  $\nabla \cdot \bar{\mathbf{u}} = 0$ , the filtered form of the conservative Allen-Cahn equation can be further rearranged as

$$\frac{\partial \bar{\phi}}{\partial t} + \bar{\nabla} \cdot (\bar{\phi} \bar{\mathbf{u}}) + \tau_\phi = \bar{\nabla} \cdot [M(\bar{\nabla} \bar{\phi} - \lambda \bar{\mathbf{n}})] \quad (44)$$

with  $\tau_\phi = \bar{\nabla} \cdot (\bar{\phi} \bar{\mathbf{u}}) - \bar{\mathbf{u}} \bar{\nabla} \cdot \bar{\phi}$  the interfacial subgrid term. According to Chesnel *et al.* [49], except for the atomization area, the contribution of the interfacial terms to the total subgrid scale terms of the LES transport equation is very small. Thus, one can simply omit this term without considerable loss of accuracy, and the filtered conservative Allen-Cahn equation can be written as

$$\frac{\partial \bar{\phi}}{\partial t} + \bar{\nabla} \cdot (\bar{\phi} \bar{\mathbf{u}}) = \bar{\nabla} \cdot [M(\bar{\nabla} \bar{\phi} - \lambda \bar{\mathbf{n}})]. \quad (45)$$

In addition to the conservative Allen-Cahn equation for interface capturing, the momentum equation including the surface tension and body force can be filtered as

$$\begin{aligned} \frac{\partial(\rho \bar{\mathbf{u}})}{\partial t} + \bar{\nabla} \cdot (\rho \bar{\mathbf{u}} \bar{\mathbf{u}}) &= -\bar{\nabla} \bar{p} + \bar{\nabla} \cdot [\mu(\bar{\nabla} \bar{\mathbf{u}} + \bar{\nabla} \bar{\mathbf{u}}^T)] \\ &\quad - \rho \bar{\nabla} \cdot \tau_{\text{SGS}} + \bar{\mu}_\phi \bar{\nabla} \bar{\phi} + \bar{\mathbf{G}}, \end{aligned} \quad (46)$$

where  $\tau_{\text{SGS}} = \bar{\mathbf{u}} \bar{\mathbf{u}} - \bar{\mathbf{u}} \bar{\mathbf{u}} = -2\nu_t(\bar{\nabla} \bar{\mathbf{u}} + \bar{\nabla} \bar{\mathbf{u}}^T)$  is the Reynolds stress with  $\nu_t$  being the subgrid kinematic viscosity.

### 2. Filtered form of discrete Boltzmann equations

When the filtering operation is employed, the filtered particle distribution function is assumed to approach a local filtered equilibrium distribution, which can be chosen to depend only on local filtered mean quantities. Here, the filtered form of discrete LBE corresponding to the Navier-Stokes equations is written as

$$\begin{aligned} \bar{g}_i(\mathbf{x} + \mathbf{e}_i \delta_t, t + \delta_t) - \bar{g}_i(\mathbf{x}, t) \\ = -(\mathbf{\Gamma}^{-1} \mathbf{\Lambda}^+ \mathbf{\Gamma})_{ij} [\bar{g}_j(\mathbf{x}, t) - \bar{g}_j^{\text{eq}}(\mathbf{x}, t)] + \delta_t (\mathbf{I} - 0.5 \mathbf{\Lambda}^+) \bar{T}_i, \end{aligned} \quad (47)$$

where  $\bar{g}_j^{\text{eq}}$  and  $\bar{T}_i$  are the filtered equilibrium distribution function and filtered force distribution function, and  $\mathbf{\Lambda}^+$  is the updated diagonal relaxation matrix considering the eddy kinematic viscosity due to the coupling of LES. Thus according to Eq. (34), the updated relaxation parameter  $s'_5$  can be calculated as

$$s'_5 = 1/\tau_{g,\text{total}} = 1 / \left( \frac{\nu + \nu_t}{c_s^2 \delta_t} + 0.5 \right). \quad (48)$$

In the calculation of viscosity in Eq. (48), the first term  $\nu$  is the physical kinematic viscosity and the second term  $\nu_t$  is the eddy kinematic viscosity. Adopting the standard Smagorinsky approach [50], the eddy kinematic viscosity is determined by

$$\nu_t = (C_s \Delta x)^2 |\bar{S}|, \quad (49)$$

where  $C_s$  is the Smagorinsky constant,  $\Delta x$  is the filter width, namely grid spacing, and  $|\bar{S}|$  is the magnitude of strain rate tensor, which is calculated by

$$|\bar{S}| = \frac{\sqrt{\tau_g^2 + \frac{18\sqrt{2}Q(C_s \Delta x)^2}{\rho}} - \tau_g}{6(C_s \Delta x)^2}, \quad (50)$$

where  $Q$  is the nonequilibrium stress tensor, which is given as

$$Q = \Pi_{ij} \Pi_{ij} \quad (51)$$

with

$$\Pi_{ij} = \sum_\alpha e_{\alpha i} e_{\alpha j} (g_\alpha - g_\alpha^{\text{eq}}). \quad (52)$$

In the same way, the filtered form of the discrete Boltzmann equation of the conservative Allen-Cahn equation is written as

$$\begin{aligned} \bar{f}_i(\mathbf{x} + \mathbf{e}_i \delta t, t + \delta t) - \bar{f}_i(\mathbf{x}, t) \\ = -(\mathbf{M}^{-1} \mathbf{S} \mathbf{M})_{ij} [\bar{f}_j(\mathbf{x}, t) - \bar{f}_j^{\text{eq}}(\mathbf{x}, t)] + \delta_t (\mathbf{I} - 0.5 \mathbf{S}) \bar{R}_i. \end{aligned} \quad (53)$$

Except for the kinematic viscosity and density, other macroscopic quantities such as order parameter, velocity, and pressure are filtered by

$$\bar{\phi} = \sum_i \bar{f}_i, \quad (54)$$

$$\rho \bar{\mathbf{u}} = \sum_i \mathbf{e}_i \bar{g}_i + 0.5 \delta_t (\bar{\mu} \bar{\nabla} \bar{\phi} + \bar{\mathbf{G}}), \quad (55)$$

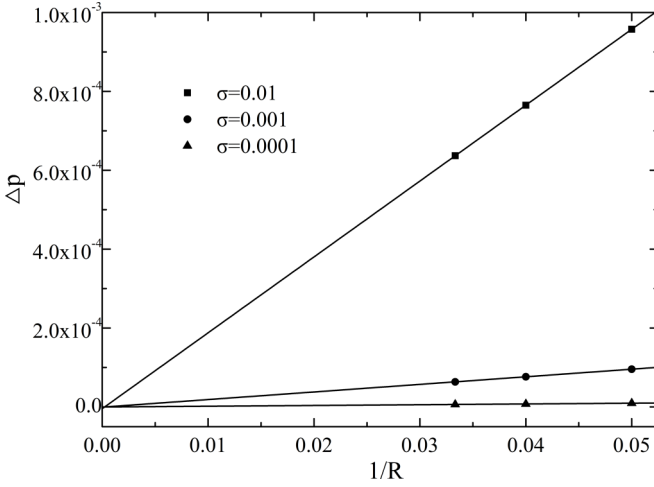


FIG. 3. Numerical validation by Laplace's law.

$$\bar{p} = \frac{c_s^2}{1 - \omega_0} \left[ \sum_{i \neq 0} \bar{g}_i + 0.5 \delta_i (\rho_l - \rho_v) \bar{\mathbf{u}} \cdot \nabla \bar{\phi} + \rho s_0(\bar{\mathbf{u}}) \right]. \quad (56)$$

$$\phi(x, y, z) = \frac{\phi_l + \phi_v}{2} + \frac{\phi_l - \phi_v}{2} \tanh \left[ \frac{2}{W} \left( R_0 - \sqrt{(x - LX/2)^2 + (y - LY/2)^2 + (z - LZ/2)^2} \right) \right], \quad (57)$$

where  $R_0$  is the initial radius of the droplet and  $W$  is the width of the phase interface. When the system reaches a steady state, the pressure difference across the interface of a three-dimensional droplet can be calculated as

$$\Delta p = \frac{2\sigma}{R}, \quad (58)$$

where  $\sigma$  is the surface tension coefficient and  $R$  is the droplet radius.

Three surface tension coefficients at different droplet radii of 20, 25, and 30 are considered. Figure 3 quantitatively compares the present numerical results with the analytical solutions. It can be seen that the numerical results agree well with the linear fit denoted by the solid lines.

According to Eqs. (57) and (16), one can drive the corresponding density profile as

$$\rho(x, y, z) = \frac{\rho_l + \rho_v}{2} + \frac{\rho_l - \rho_v}{2} \tanh \left[ \frac{2}{W} \left( R - \sqrt{(x - LX/2)^2 + (y - LY/2)^2 + (z - LZ/2)^2} \right) \right]. \quad (59)$$

Thus, the analytical density distribution can be obtained. Figure 4 depicts the density distribution as a function of the distance from the droplet center. The solid line is the values corresponding to the analytic solution; two different symbols are the numerical results obtained by adopting the MRT operator and SRT operator for comparison. To quantitatively describe the accuracy of the two models, the following relative error is used:

$$E_\rho = \frac{\sum_x |\rho_x^n(x) - \rho_x^a(x)|}{\sum_x |\rho_x^a(x)|}, \quad (60)$$

where the superscripts  $n$  and  $a$  denote the numerical and analytical solutions. The values of  $E_\rho$  for MRT and SRT models are 0.25% and 0.49%, respectively. In addition, the changes of the maximal kinetic energy obtained by the MRT and SRT

### III. SIMULATIONS AND DISCUSSIONS

Three-dimensional simulations require massive computational resources. Considering the efficient parallel performance, the three-dimensional model has been coded with the Message Passing Interface (MPI) parallel library in the following simulations.

In this section, four benchmark cases, including stationary droplet, spinodal decomposition, Rayleigh-Taylor instability, and droplet splashing on a thin liquid film, are simulated to validate the present three-dimensional LB-LES multiphase model. Attempts have been made to conduct detailed comparisons between the simulation results and the analytical solutions or the available results in previous studies. Finally, the jet-breakup phenomenon is investigated and different breakup regimes are presented and discussed.

#### A. Stationary droplet

At the initialization, a droplet suspends in the vapor phase in an  $80 \times 80 \times 80$  lattices system. The periodic boundary is applied in all directions. The density ratio of the liquid phase to the vapor phase is set to be 1000. The distribution of the order parameter is given as

operators at early times are compared in Fig. 5. Here, the maximal kinetic energy is calculated as  $E_{\max} = \rho |\mathbf{u}|^2 / 2$ , and the dimensionless time  $t^*$  is defined as  $t^* = t\sigma / (\rho_v \nu_v R)$ . As shown in Fig. 5, for the MRT model, the  $E_{\max}$  varies from  $10^{-13}$  to  $10^{-11}$  at the initial stage and reaches a steady value with a magnitude of  $10^{-12}$ , while for the SRT model, it ranges  $10^{-12}$ – $10^{-10}$  and reaches a steady value with a magnitude of  $10^{-10}$ .

The spurious velocity around the interface is a commonly concerned problem in LB approaches for two-phase flows. In the current study, the spurious velocity is computed by  $u_s = \sqrt{u_x^2 + u_y^2 + u_z^2}$ , where  $u_x$ ,  $u_y$ , and  $u_z$  are the maximum velocity value in three dimensions. The numerical experiments indicate that the spurious velocities are  $1.51 \times 10^{-7}$  and  $3.36 \times 10^{-6}$  for the MRT and SRT models with a density ratio of 1000. It has been reported that the maximum amplitude

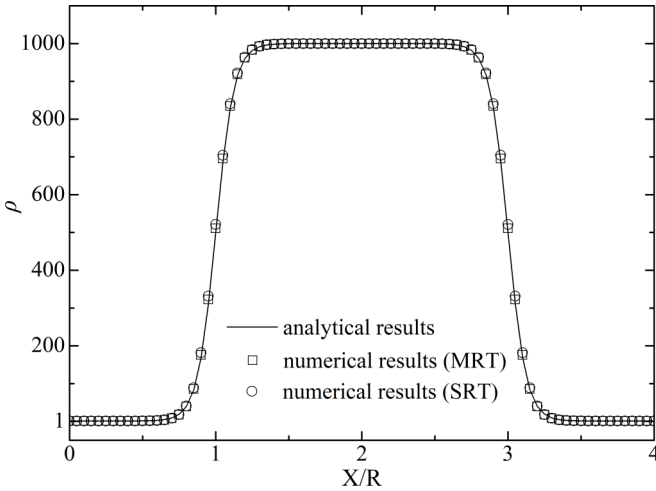


FIG. 4. Density profiles at  $y = LY/2$  and  $z = LZ/2$ .

of spurious velocities in an improved Shan-Chen model [5] has the order of  $10^{-3}$ . Recently, Ba *et al.* [51] developed an improved color-gradient-based LB model for high density ratios, which produced spurious velocities with the order of  $10^{-5}$ . As for the Cahn-Hilliard type of LB model [10], they can obtain spurious velocities at the level of  $10^{-6}$ . From the above discussion, it can be concluded that the present LB model can produce relatively small spurious velocities.

**B. Spinodal decomposition**

Spinodal decomposition, also referred to as the separation of phases and components, is an important property of mixtures of immiscible fluids [9]. This example focuses on the demonstration of the capability of the model in simulating phase separation, and the growth of the domain size with time is investigated quantitatively. The phase separation is divided into nucleation growth and spinodal decomposition in the classical dynamic theory of phase separation. The dynamic behavior of spinodal decomposition is scaled by the domain size. If the inertial term in the Navier-Stokes equation dominates the viscous term (the viscosity is small), a  $t^{2/3}$  growth

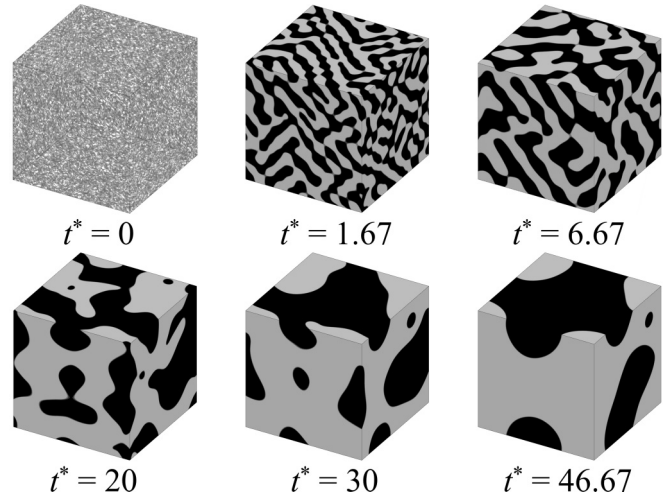


FIG. 6. Separation of binary fluid: distribution of order parameters shown in grayscale.

law can be obtained to describe the growth of the domain size [52–54]. The  $t^{2/3}$  growth law has been reported in several numerical simulations, such as Ginzburg-Landau models [55], dissipative particle dynamics [56], and lattice Boltzmann models [57,58].

In this section, the separation of mixed fluid is simulated in an  $80 \times 80 \times 80$  lattice system by using the present model. At the initial state, the order parameter is treated as a random distribution with perturbation of 1% around 0.5, which reads as

$$\phi(x, y, z) = 0.5 + \left(0.001 - \frac{\text{rand}\%10}{10000}\right), \quad (61)$$

where  $\text{rand}\%10$  is the remainder obtained via a random number divided by 10. The surface tension coefficient is set as 0.1 for a fast separation. The interface width is fixed at  $W = 3$ . The velocity is zero in the whole domain, and the viscosity ratio and the density ratio are 1 and 1000, respectively. Figure 4 shows the evolution process of the spinodal decomposition, in which the separation of different phases can

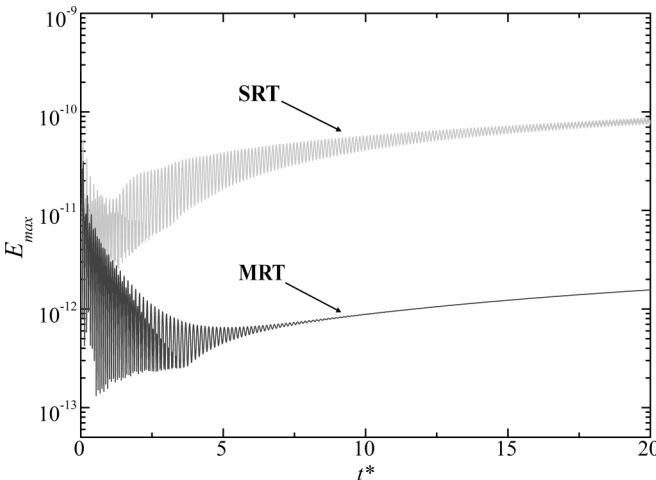


FIG. 5. Maximum kinetic energy versus time.

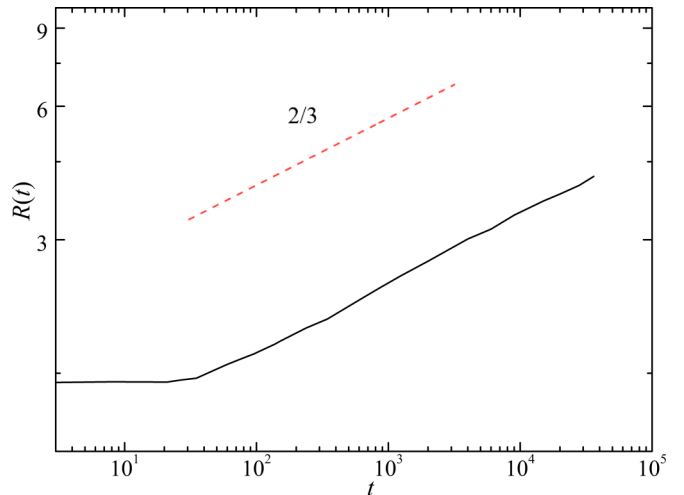


FIG. 7. The domain size  $R$  versus time step  $t$ .



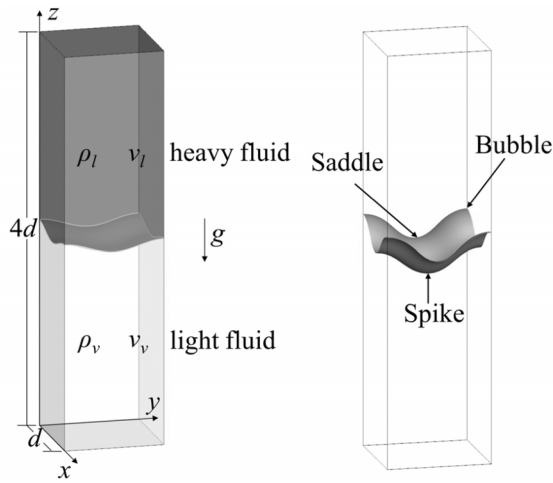


FIG. 8. Schematic diagram for the Rayleigh-Taylor instability.

be observed. Here, the dimensionless time is normalized by  $t^* = t\sigma / (\rho_l \nu_l W)$ . The spinodal decomposition process takes a pretty long time cycle for complete phase separation in three dimensions. And it takes more time in the late period than the beginning. The order parameter is almost 1.0 and 0 for the two phases at the time of 46.67, as presented in Fig. 6. Foreseeably, the final form of separation should be expressed as a sphere suspending in another phase.

To quantify the domain coarsening rate succinctly and effectively, the time evolution of the domain size is calculated using the standard “broken bond” method [58–60]. Using this method, the domain size is calculated as

$$R(t) = \frac{V}{N_x + N_y + N_z}, \quad (62)$$

where  $V$  is the volume of the system and  $N_i$  ( $i = x, y, z$ ) is the total number of pairs of nearest neighbor sites with one order parameter larger than 0.5 and another smaller than 0.5 in the  $i$  direction. Figure 7 shows the logarithm of the domain size  $R(t)$  as a function of the logarithm of the time steps. The dotted line corresponds to a growth exponent  $2/3$  and it serves as a guide to the eye only. The simulation result shows a good agreement with the  $R(t) \sim t^{2/3}$  growth law.

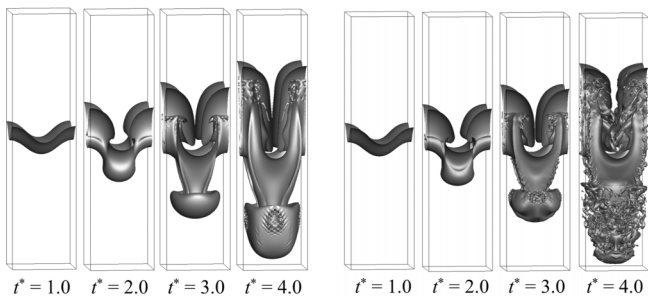


FIG. 9. Snapshots of the interface evolution at  $Re = 1024$  (left) and  $Re = 10000$  (right).

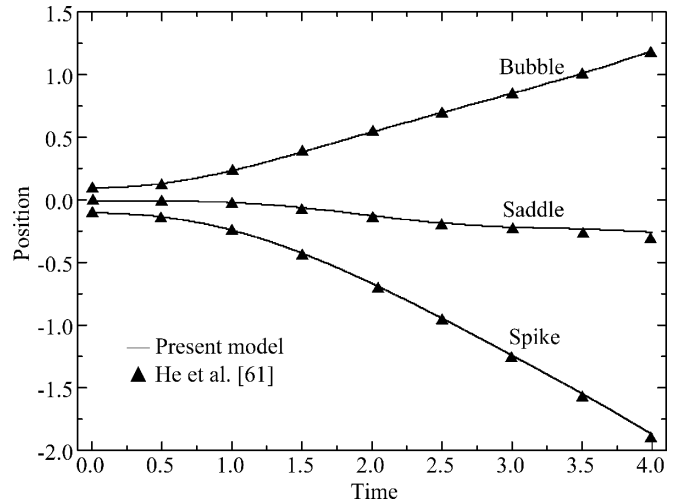


FIG. 10. Comparison of the bubble, saddle, and spike front positions at  $Re = 1024$  between present results and those of He *et al.* [61].

### C. Rayleigh-Taylor instability

In this section, a benchmark problem of the Rayleigh-Taylor instability (RTI) is simulated. The RTI is a classical and common instability phenomenon, which involves complex interfacial interactions [61]. Figure 8 sketches the schematic diagram for RTI and the positions of bubble, saddle, and spike. As shown in Fig. 8, a layer of heavy fluid with density  $\rho_l$  is located on the top of the light one with density  $\rho_v$ . As stated in Ref. [18], any disturbance at the interface can be accelerated by gravity to produce downward-moving spikes of heavy fluid and upward-moving bubbles of light fluid. This is the so-called RTI, a crucial type of instability that is responsible for interface destabilization. The simulation is implemented in a three-dimensional (3D) domain of size  $d \times d \times 4d$  with periodic and no-slip boundary conditions in the streamwise and normal-wall directions, respectively. The characteristics of this phenomenon are governed by two nondimensional parameters of the Reynolds number and the Atwood number, which can be defined as  $Re = d^{3/2}g^{1/2}/\nu$  and  $At = (\rho_l - \rho_v)/(\rho_l + \rho_v)$ , respectively. Here,  $d$  is the characteristic length or wavelength, and  $g$  is the gravity acceleration, as depicted in Fig. 8. The time is normalized as  $t^* = t/\sqrt{d/g}$ .

At the initial time, the order parameter profile, that distributes smoothly across the interface with an amplitude of  $0.05d$ , is given as

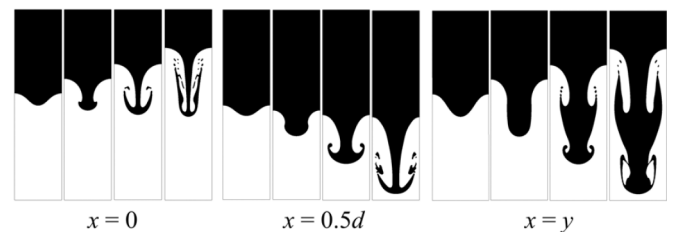


FIG. 11. Evolution of the fluid interface at the planes of  $x = 0$ ,  $x = 0.5d$ , and  $x = y$  ( $t^* = 1.0, 2.0, 3.0$ , and  $4.0$  from left to right).

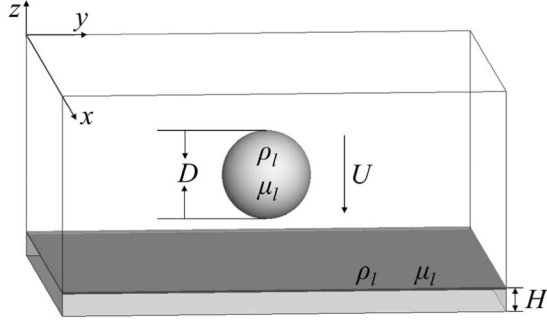


FIG. 12. Schematic diagram for a droplet splashing on a thin liquid film.

$$\phi(x, y, z) = \frac{\phi_l + \phi_v}{2} + \frac{\phi_l - \phi_v}{2} \tanh \left\{ \frac{2}{W} \left[ z - 0.05d \right. \right. \\ \left. \left. \times \left( \cos \frac{2\pi x}{d} + \cos \frac{2\pi y}{d} \right) - 2d \right] \right\}, \quad (63)$$

where the interface width  $W$  is fixed at 4. In the simulation, the computational domain is  $128 \times 128 \times 512$ , and the key parameters are fixed as  $At = 0.5$  and  $\sqrt{gd} = 0.04$ . The surface tension coefficient is set to be  $10^{-4}$ , and the viscosity ratio is 1.0. To incorporate the gravitational effect, the following body force  $\mathbf{G}$  in the  $z$  direction is applied to the fluids:

$$\mathbf{G} = \left[ 0 \quad 0 \quad -\left( \rho - \frac{\rho_l + \rho_v}{2} \right) g \right]. \quad (64)$$

Figure 9 gives the evolution of the fluid interface at  $Re = 1024$  and  $Re = 10000$ . It can be seen that when the  $Re$  number is 1024, the heavy fluid and the light one penetrate into each other early and then the bubble, saddle, and spike are formed due to the gravity effect. After that, the heavy fluid rolls up along the flank of the spike, and a mushroomlike structure appears, which can be attributed to the Kelvin-Helmholtz instability providing the rolling motion of the interface [27]. When the  $Re$  number is 10000, the basic morphology of the interface at  $t^* = 1.0$  and 2.0 is the same as those of  $Re = 1024$ , while at  $t^* = 3.0$  and 4.0 the interface tends to disintegrate and liquid ligaments and small droplets appear. The pattern of the liquid interface obtained by the present model compares well with the previous results [62,63]. In Fig. 10, the front positions of the bubble, saddle, and spike at  $Re = 1024$  are plotted, and the curves are compared with the results of He *et al.* [61]. It can be seen that the two results are in good agreement, which verifies the ability of the current coupled LB-LES model to simulate three-dimensional unsteady multiphase flows.

To track more closely the interface evolution, Fig. 11 further presents the evolution of the fluid interface at the diagonal vertical plane  $x = y$  and the vertical planes  $x = 0$  and  $x = 0.5d$  at  $Re = 1024$ . The interfaces in the vertical planes  $x = 0$  and  $x = 0.5d$  are similar to those in the two-dimensional RTI [12,27]. The heavy-fluid stem and roll-up at the plane of  $x = 0$  is smaller than those at  $x = 0.5d$ . However, the interface at the plane of  $x = y$  is quite different. The two-layer roll-up phenomenon can be seen in this plane, which is caused by the instabilities at the spike tip and saddle point [61].

TABLE I. Parameters for four breakup regimes of liquid-liquid system.

| Case Regime | 1 dripping | 2 varicose | 3 sinuous | 4 atomization |
|-------------|------------|------------|-----------|---------------|
| Re          | 50         | 200        | 2048      | 8192          |
| Oh          | 0.019      | 0.0067     | 0.0063    | 0.022         |

#### D. Droplet splashing on a thin liquid film

In this section, the three-dimensional simulation of a droplet splashing on a thin liquid film is performed to validate the proposed model. A spherical droplet of diameter  $D$  with velocity  $U$  hits against a thin liquid film of height  $H$  in an ambient vapor field, as sketched in Fig. 12. Two nondimensional parameters are introduced to describe this phenomenon: the Reynolds number and the Weber number, which can be defined as  $Re = \rho_l U D / \mu_l$  and  $We = \rho_l U^2 D / \sigma$ , respectively, where  $\sigma$  is the surface tension coefficient. In the simulation, the density ratio and viscosity ratio are  $\rho_l / \rho_v = 1000$  and  $\mu_l / \mu_v = 40$ , respectively. The dimensionless time is normalized by  $t^* = t / (D/U)$ .

According to Rieber and Frohn [64], the radial growth of the splashing lamella can be described by the following formula:

$$\frac{r}{D} = \left( \frac{6H}{D} \right)^{-1/4} \sqrt{t^*}. \quad (65)$$

Note that in the above relation,  $t^* = 0$  is the time of the first contact between the droplet and the liquid film, and  $D$  is the droplet diameter.

In the following, two cases are simulated and the results are compared with the above relationship. The computational domain is set to be  $256 \times 256 \times 128$  lattices. For case 1, nondimensional parameters  $Re$  and  $We$  are set to be 500 and 12800, respectively. For case 2,  $Re$  and  $We$  are set to be 1000 and 8000, respectively. Figure 13 shows the evolutions of interface morphology for the droplet splashing on a thin liquid film for two cases. The dimensionless time  $t^*$  is 1.0, 1.5, 2.0, 2.5, 3.0, and 3.5 for each of these subgraphs. As can be seen from the evolution of interface morphology for case 1, a surface wave moves outwards from the impact center, and a circle of neat splashing lamella arises after the impact, while the secondary droplets are not founded. For case 2, a splashing lamella, thinner and higher than case 1, is ejected from the impact center immediately and grows radially outwards. On the top of the lamella, some breakup can be observed at  $t^* = 2.5$ . After, some small droplets separate from the lamella and splash away.

Figure 14 depicts the evolution process of the vertical cross sections at  $x = LX/2$  of the splashing lamella for case 2. The horizontal and vertical coordinates, namely the  $y$  and  $z$  directions, are scaled by droplet diameter. The time interval between two adjacent phase interface outlines is half of the dimensionless time. As can be seen from the changes of the outlines, the secondary droplets are produced symmetrically. The lamella tends to disintegrate under the action of the inertia and three-dimensional synechia effect. Figure 15 plots the

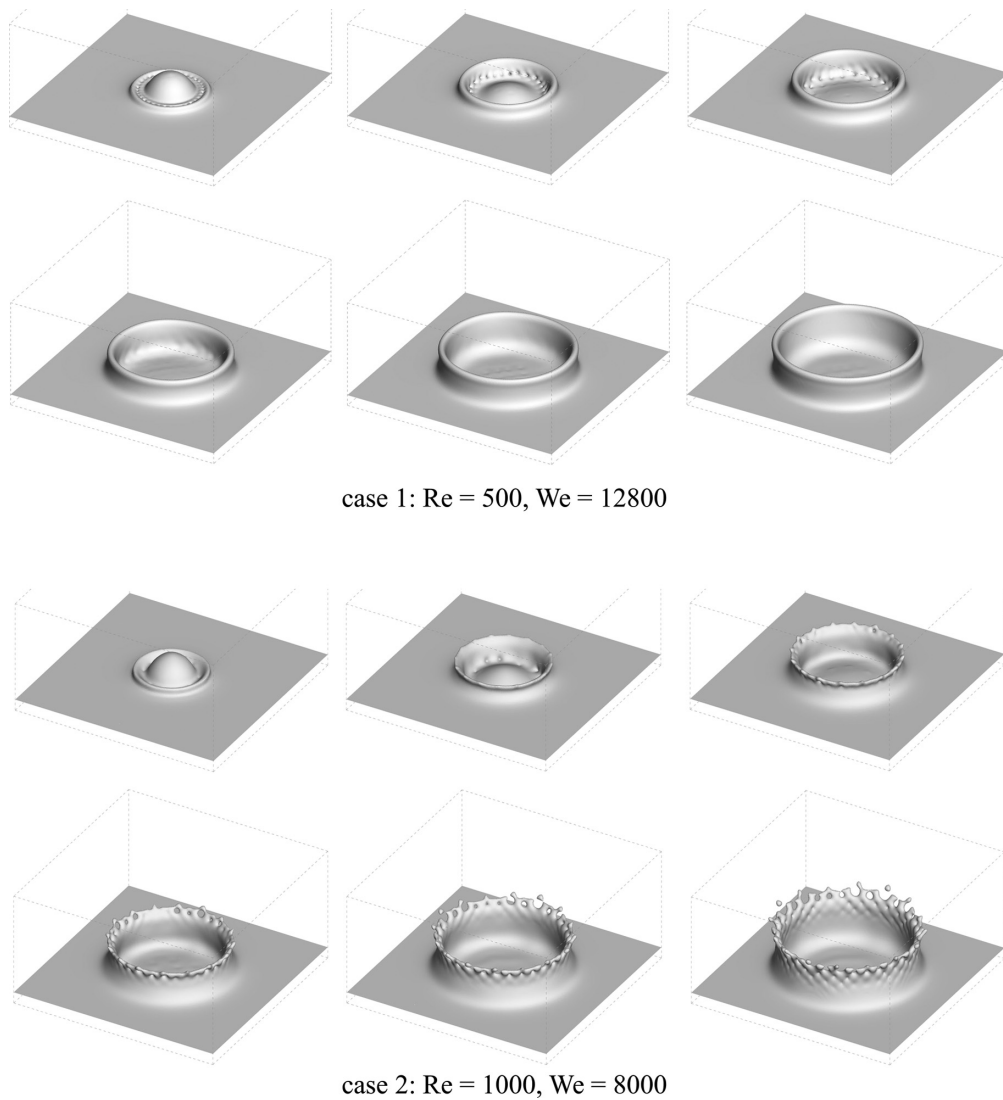


FIG. 13. Evolution of interface morphology for droplet splashing on a thin liquid film (time  $t^*$  is 1.0, 1.5, 2.0, 2.5, 3.0, and 3.5 from left to right for both cases).

evolutions of the radial distance of the splashing lamella for case 1 and case 2. The square and triangle points are the simulation results of case 1 and case 2, respectively, and the

solid line is the radial growth curve proposed in Ref. [64]. The variation trends of the simulation results conform to the relation curve.

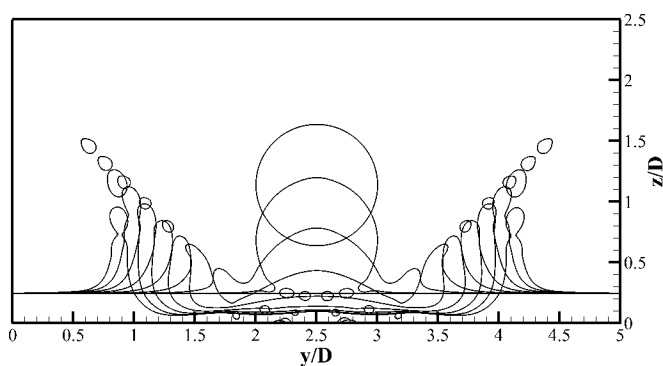


FIG. 14. Vertical cross sections of the splashing lamella for case 2.

### E. Liquid jet breakup

A liquid injected into another fluid is a typical multiphase flow, while the breakup of the liquid jet is essentially three-dimensional flow and possesses multiscale phenomena such as droplet pinch-off and atomization. According to Ohnesorge [65], the breakup regimes of the injected liquid are classified into four types: (0) dripping, (I) varicose, (II) sinuous, and (III) atomization.

In this section, different breakup regimes of the liquid-liquid system and liquid-gas system are simulated using the proposed LB-LES coupled model, respectively. Figure 16 illustrates the schematic diagram for liquid jet simulation. In the initial state, the computational domain is filled with still continuous phase. The dispersed phase in the circular area

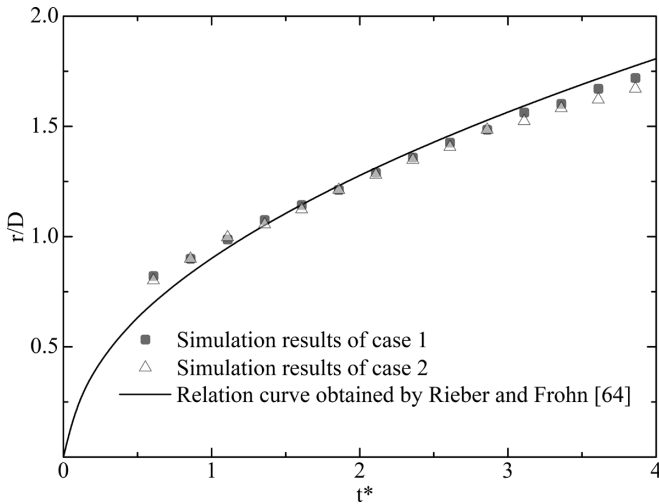


FIG. 15. Evolutions of the radial distance of splashing lamella for case 1 and case 2.

at the upper boundary is injected into the continuous phase from the inlet with the diameter of  $D$ , and the jet velocity is set as  $U$ . In the simulations, the horizontal and longitude directions are set to be the periodic boundary, and at the lower boundary, the convection outlet boundary is used [66]. Two nondimensional parameters of the Reynolds number and the Ohnesorge number are used to characterize this jet flow, which can be defined as  $Re = \rho_l U D / \mu_l = U D / \nu_l$  and  $Oh = \mu_l / \sqrt{\rho_l \sigma D}$ , respectively. It is noted that in the present study, time is nondimensionalized by the inlet diameter  $D$  and the inlet velocity  $U$  as  $t^* = \frac{t}{D/U}$ .

**1. Liquid-liquid system**

In this section, the liquid jet breakup of the liquid-liquid system is simulated in a  $120 \times 120 \times 450$  lattice system by using the proposed model. The density ratio is fixed at 2.0, and four breakup regimes are produced and located on the Oh-Re map, as depicted in Fig. 21. Nondimensional parameters of

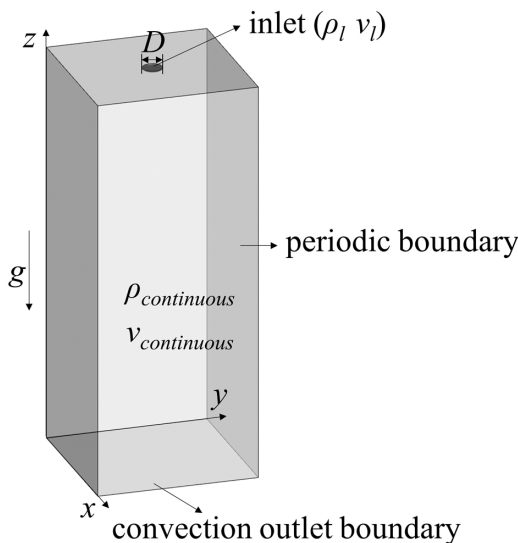


FIG. 16. Schematic diagram for liquid jet simulation.

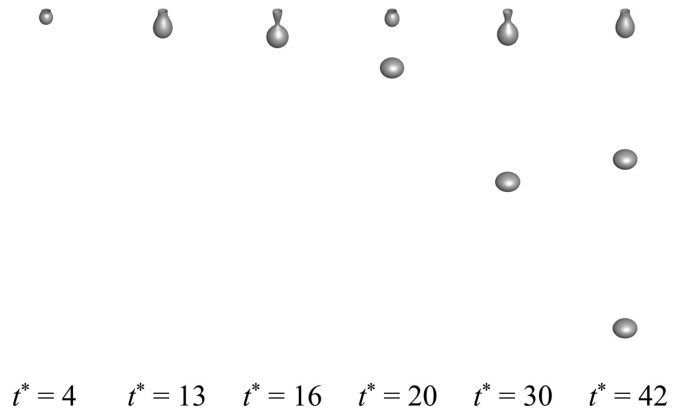


FIG. 17. Simulation results of case 1 in the dripping regime of the liquid-liquid system.

Re number, Oh number, and morphological structure of liquid phase are taken as the references to distinguish different regimes; so it is with the liquid-gas system.

Table 1 lists the parameters for four cases, corresponding to different breakup regimes. Case 1 is the simulation in the dripping regime, as given in Fig. 17. As  $t^*$  is about 16, the first droplet is almost formed. Under the action of gravity and surface tension, the droplet disconnects from the liquid column and falls downward. The pinch-off effect can be observed at the joint, which is caused by surface tension [67]. After the first droplet falls off, the second droplet begins to form and falls eventually at about  $t^* = 30$ . Figure 18 shows the liquid jet breakup in the varicose regime labeled by case 2. Different from case 1, the liquid column in case 2 is very long. In the process of the liquid column growth, some droplets separate from the end of the liquid column constantly. As can be seen from Fig. 18, the dispersed phase shows a distinct asymmetry, and velocities perpendicular to the vertical direction appear. Furthermore, this asymmetry and instability are obvious in sinuous and atomization regimes.

Figure 19 displays the interface evolution of case 3 in the sinuous regime. It is found out that a mushroomlike head shape appears at the beginning. At  $t^* = 15$ , a significant interface instability emerges at the front of the liquid column.

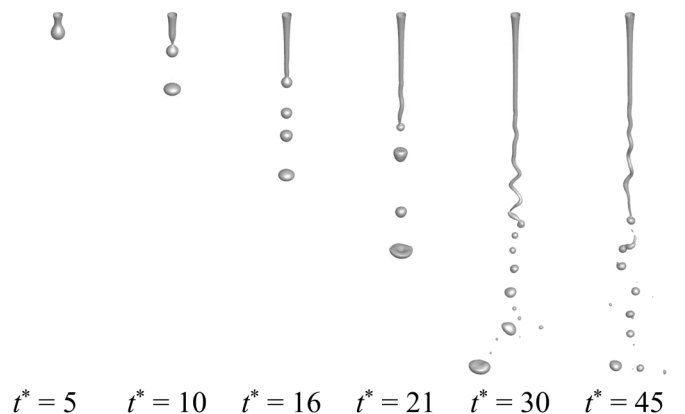


FIG. 18. Simulation results of case 2 in the varicose regime of the liquid-liquid system.

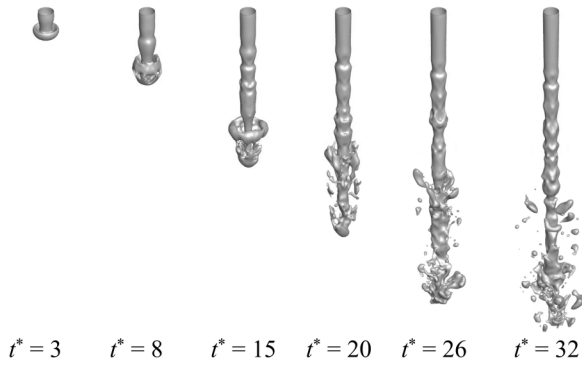


FIG. 19. Simulation results of case 3 in the sinuous regime of the liquid-liquid system.

Part of the dispersed phase falls off and forms liquid filament or droplets. At  $t^* = 26$ , a further breakup occurs at the top of the liquid column, and many droplets are generated due to interface instability. According to Saito *et al.* [68], this interfacial instability is triggered by the return flow of the mushroom head generated in the initial stage of jet injection, although no artificial spatial or temporal perturbation has been assumed in the initial or boundary conditions. The atomization regime is exhibited in Fig. 20. Similar to case 3, a mushroomlike head appears at the early stage, then the dispersed phase begins to break. A mass of tiny droplets and irregular liquid silk peel away from the dispersed phase. Compared with case 3, more and smaller tiny droplets with a wider jet scope are produced. And in detail, the liquid column is mainly composed of many deformed liquid filaments, and its surrounding and internal clearance are filled with many small droplets.

In Fig. 21, the locations of four cases in different regimes are pointed out on the Oh-Re map, which is proposed by Saito *et al.* [69]. Case 1 and case 2 are in the dripping or varicose area, case 3 and case 4 are in the sinuous and atomization area, respectively. Different areas are separated by dashed lines. The characteristics of dripping (regime 0), varicose breakup (regime I), sinuous breakup (regime II), and atomization (regime III) are successfully simulated.

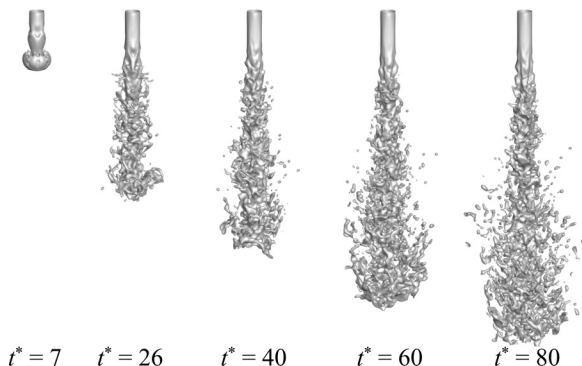


FIG. 20. Simulation results of case 4 in the atomization regime of the liquid-liquid system.

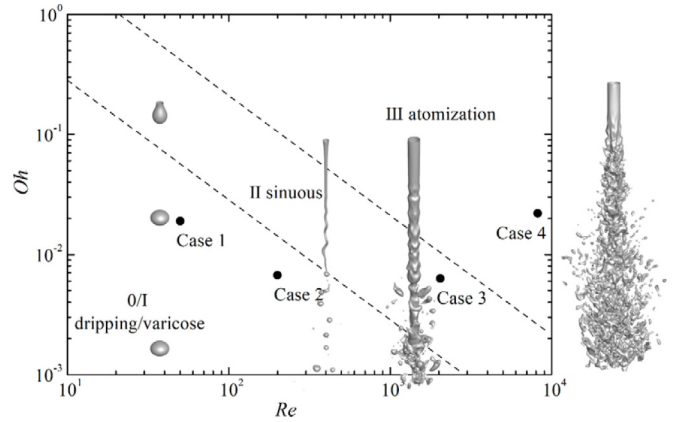


FIG. 21. Locations of four cases on the Oh-Re map of the liquid-liquid system proposed by Saito *et al.* [69].

### 2. Liquid-gas system

In this section, the liquid jet breakup of the liquid-gas system is simulated in a  $120 \times 120 \times 450$  lattice system. The density ratio is fixed at 200.0, and different cases in the varicose regime, sinuous regime, and atomization regime are produced and pointed out on the Oh-Re map. Table II lists the parameters used in the simulations. The maximum Re number in this study reaches  $10^4$ , which fully confirms the performance of this three-dimensional multiphase LB-LES model at a high Reynolds number.

Figures 22–24 present the three cases in different breakup regimes, respectively. As can be seen from Figs. 22 and 18, the two cases in the varicose regime of the liquid-gas system and the liquid-liquid system are similar. For the cases in the sinuous regime and atomization regime of the liquid-gas system, as shown in Fig. 23 and Fig. 24, the mushroomlike head no longer appears at the early stage. More and smaller independent droplets are produced compared with cases in the liquid-liquid system, and the head of the liquid column shows a complete decomposition state. By comparing the liquid phase structure of case 3 in the atomization regime and case 2 in the sinuous regime, some details are different. First, the liquid column obtained in the former is shorter than that in the latter, which means the liquid phase disintegrates early in the former. Second, there are more and smaller droplets produced in the former than in the latter. Third, the atomization angle is larger in the atomization regime than that in the sinuous regime. The liquid phase structure combined with the parameters Re and Oh is important proof to distinguish the above two regimes.

Analogously, the locations of the above three cases on the Oh-Re map of the liquid-gas system are displayed in

TABLE II. Parameters for different breakup regimes of liquid-gas system.

| Case   | 1        | 2       | 3           |
|--------|----------|---------|-------------|
| Regime | varicose | sinuous | atomization |
| Re     | 1000     | 6000    | 10240       |
| Oh     | 0.002    | 0.007   | 0.02        |

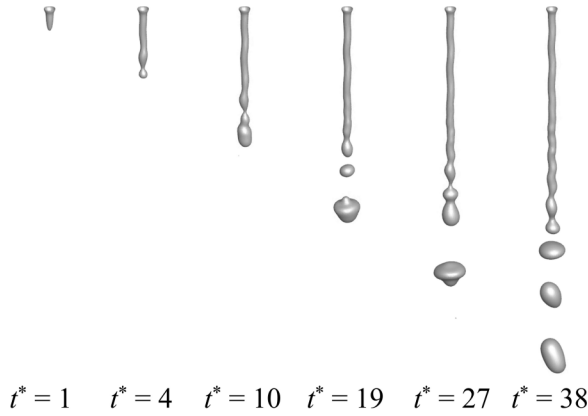


FIG. 22. Simulation results of case 1 in the varicose regime of the liquid-gas system.

Fig. 25, which is obtained by Kolev [70]. Two dashed lines are outlined to be the boundaries of regime 0/I, II, and III, and the phase interface contour maps of the three cases are pasted beside. A conclusion can easily be drawn that a large density ratio or a high Re number enhances the breakup process. The liquid jet disintegrates more thoroughly at a larger density ratio compared with the liquid-liquid system. More and smaller tiny droplets can be produced at a higher Re number in the atomization regime compared with the sinuous regime.

On the Oh-Re map of the liquid-liquid system, as shown in Fig. 21, the ranges of Re and Oh are  $10-10^4$  and  $10^{-3}-1$ . For the liquid-gas system, the ranges of Re and Oh are  $50-10^5$  and  $5 \times 10^{-4}-0.2$ , as displayed in Fig. 25. There is no direct correlation between Re number, Oh number, and different breakup regimes. Compared with the liquid-liquid system, the value of the Re number is larger in the liquid-gas system, while for the Oh number, its value is smaller than that in the liquid-liquid system. Different physical properties of the continuous phase show different shear forces

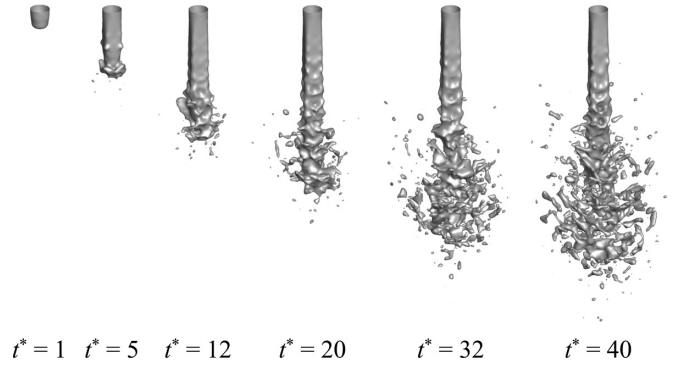


FIG. 23. Simulation results of case 2 in the sinuous regime of the liquid-gas system.

on the dispersed phase. In general, for the liquid-gas system, a higher Re number and a smaller Oh number are needed to achieve different regimes than in the liquid-liquid system.

Given the difficulty for the simulation of liquid jet breakup in two-phase flow, this case is used to examine the stability of the present model. As summarized in Table III, the density ratios and Re numbers used in the studies of Saito *et al.* [68] and Amirshaghghi *et al.* [38] are listed, and their values in the stability test of the present 3D MRT model only and the present coupled LB-LES model are given. In the study of Saito *et al.* [68], the density ratio is 1.4, and the maximum Re number is 3400. In the study of Amirshaghghi *et al.* [38], the Re number can reach 6000 when the density ratio is 100, and the Re number is set 2000 at the density ratio of 250. While in our tests for the present coupled LB-LES model, the Re number can reach more than 10 000 at the density ratio of 200. Consequently, the present coupled LB-LES model has a significant improvement in stability at large density ratios and high Re numbers compared with the present 3D MRT model only and the previous studies.

TABLE III. Comparison of model stability among the previous studies, the present MRT model only, and the present coupled LB-LES model at different density ratios and Re numbers.

| Work                                                     | Density ratio | Re number | Stability  |
|----------------------------------------------------------|---------------|-----------|------------|
| Numerical results of Saito <i>et al.</i> [68]            | 1.4           | 3400      |            |
| Numerical results of Amirshaghghi <i>et al.</i> [38]     | 40            | 3000      |            |
|                                                          | 100           | 6000      |            |
|                                                          | 250           | 2000      |            |
|                                                          |               |           |            |
| The present results obtained by the 3D MRT model only    | 1             | 8000      | convergent |
|                                                          | 200           | 1000      | convergent |
|                                                          |               | 2500      | divergent  |
|                                                          | 600           | 500       | convergent |
|                                                          |               | 1500      | divergent  |
|                                                          | 1000          | 100       | convergent |
| The present results obtained by the coupled LB-LES model |               | 500       | divergent  |
|                                                          | 200           | 15 000    | convergent |
|                                                          | 600           | 5000      | convergent |
|                                                          |               | 10 000    | divergent  |
|                                                          | 1000          | 3000      | convergent |
|                                                          | 8000          | divergent |            |

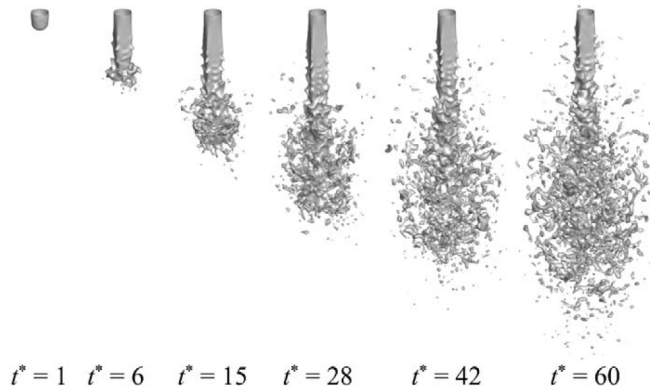


FIG. 24. Simulation results of case 3 in the atomization regime of the liquid-gas system.

#### IV. CONCLUSIONS

In this work, a coupled three-dimensional LB-LES model is proposed for modeling multiphase flow at large density ratios and high  $Re$  numbers. The MRT collision operator is applied for the LB scheme, and the Smagorinsky approach is used to perform the filtering operation. The conservative Allen-Cahn equation is discretized to track the phase interface in the framework of the LBM. Then the Rayleigh-Taylor instability and the phenomenon of droplet splashing on a thin liquid film are carried out. The simulation results are in good agreement with the previous studies and the analytical solutions, respectively. Finally, different regime cases in the liquid

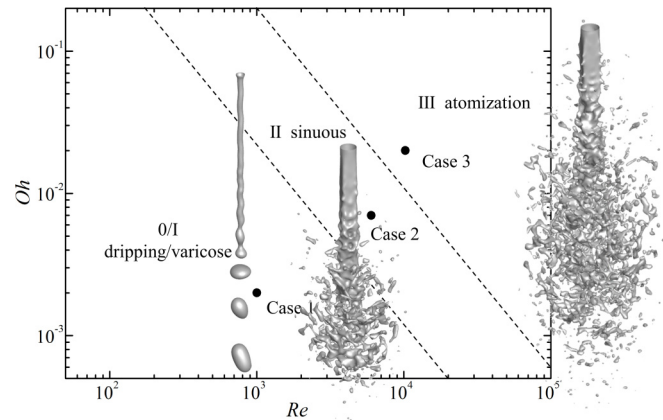


FIG. 25. Locations of three cases on the Oh-Re map of the liquid-gas system proposed by Kolev [70].

jet breakup process of the liquid-liquid system and liquid-gas system are simulated, respectively. The maximum value of the  $Re$  number can reach 10 240, and the proposed model shows a good performance in simulating three-dimensional multiphase flows at a high  $Re$  number.

#### ACKNOWLEDGMENTS

This work was jointly supported by the National Natural Science Foundation of China under Grant No. 51776031 and the Fundamental Research Funds for the Central Universities under Grant No. DUT19LAB04.

- 
- [1] M. C. Sukop and D. T. Thorne, *Lattice Boltzmann Modeling: An Introduction for Geoscientists and Engineers* (Springer, Berlin, 2006).
- [2] C. K. Aidun and J. R. Clausen, Lattice-boltzmann method for complex flows, *Annu. Rev. Fluid Mech.* **42**, 439 (2010).
- [3] T. Reis and T. N. Phillips, Lattice boltzmann model for simulating immiscible two-phase flows, *J. Phys. A: Math. Theor.* **40**, 4033 (2007).
- [4] H. Liu, A. J. Valocchi, and Q. Kang, Three-dimensional lattice boltzmann model for immiscible two-phase flow simulations, *Phys. Rev. E* **85**, 046309 (2012).
- [5] Z. Yu and L.-S. Fan, Multirelaxation-time interaction-potential-based lattice boltzmann model for two-phase flow, *Phys. Rev. E* **82**, 046708 (2010).
- [6] Q. Li, K. Luo, and X. Li, Lattice boltzmann modeling of multiphase flows at large density ratio with an improved pseudopotential model, *Phys. Rev. E* **87**, 053301 (2013).
- [7] A. Xu, G. Gonnella, and A. Lamura, Morphologies and flow patterns in quenching of lamellar systems with shear, *Phys. Rev. E* **74**, 011505 (2006).
- [8] C. Pooley and K. Furtado, Eliminating spurious velocities in the free-energy lattice boltzmann method, *Phys. Rev. E* **77**, 046702 (2008).
- [9] Y. Zu and S. He, Phase-field-based lattice boltzmann model for incompressible binary fluid systems with density and viscosity contrasts, *Phys. Rev. E* **87**, 043301 (2013).
- [10] H. Liang, B. Shi, Z. Guo, and Z. Chai, Phase-field-based multiple-relaxation-time lattice boltzmann model for incompressible multiphase flows, *Phys. Rev. E* **89**, 053320 (2014).
- [11] G. Tang, H. Xia, and Y. Shi, Study of wetting and spontaneous motion of droplets on microstructured surfaces with the lattice boltzmann method, *J. Appl. Phys.* **117**, 244902 (2015).
- [12] E. Dinesh Kumar, S. Sannasiraj, and V. Sundar, Phase field lattice boltzmann model for air-water two phase flows, *Phys. Fluids* **31**, 072103 (2019).
- [13] J. W. Cahn and J. E. Hilliard, Free energy of a nonuniform system. i. interfacial free energy, *J. Chem. Phys.* **28**, 258 (1958).
- [14] J. W. Cahn and J. E. Hilliard, Free energy of a nonuniform system. iii. nucleation in a two-component incompressible fluid, *J. Chem. Phys.* **31**, 688 (1959).
- [15] O. Penrose and P. C. Fife, Thermodynamically consistent models of phase-field type for the kinetic of phase transitions, *Physica D (Amsterdam, Neth.)* **43**, 44 (1990).
- [16] V. E. Badalassi, H. D. Cenicerros, and S. Banerjee, Computation of multiphase systems with phase field models, *J. Comput. Phys.* **190**, 371 (2003).
- [17] Q. Li, K. H. Luo, Q. Kang, Y. He, Q. Chen, and Q. Liu, Lattice boltzmann methods for multiphase flow and phase-change heat transfer, *Prog. Energy. Combust. Sci.* **52**, 62 (2016).
- [18] X. He, S. Chen, and R. Zhang, A lattice boltzmann scheme for incompressible multiphase flow and its application in

- simulation of rayleigh–taylor instability, *J. Comput. Phys.* **152**, 642 (1999).
- [19] T. Lee and C.-L. Lin, A stable discretization of the lattice boltzmann equation for simulation of incompressible two-phase flows at high density ratio, *J. Comput. Phys.* **206**, 16 (2005).
- [20] H. Zheng, C. Shu, and Y.-T. Chew, A lattice boltzmann model for multiphase flows with large density ratio, *J. Comput. Phys.* **218**, 353 (2006).
- [21] T. Lee and L. Liu, Lattice boltzmann simulations of micron-scale drop impact on dry surfaces, *J. Comput. Phys.* **229**, 8045 (2010).
- [22] M. Geier, A. Fakhari, and T. Lee, Conservative phase-field lattice boltzmann model for interface tracking equation, *Phys. Rev. E* **91**, 063309 (2015).
- [23] H. Wang, Z. Chai, B. Shi, and H. Liang, Comparative study of the lattice boltzmann models for allen-cahn and cahn-hilliard equations, *Phys. Rev. E* **94**, 033304 (2016).
- [24] A. Begmohammadi, R. Haghani-Hassan-Abadi, A. Fakhari, and D. Bolster, Study of phase-field lattice boltzmann models based on the conservative allen-cahn equation, *Phys. Rev. E* **102**, 023305 (2020).
- [25] Z. Chai, D. Sun, H. Wang, and B. Shi, A comparative study of local and nonlocal allen-cahn equations with mass conservation, *Int. J. Heat. Mass. Transfer* **122**, 631 (2018).
- [26] H. Liang, J. Xu, J. Chen, H. Wang, Z. Chai, and B. Shi, Phase-field-based lattice boltzmann modeling of large-density-ratio two-phase flows, *Phys. Rev. E* **97**, 033309 (2018).
- [27] X. Zhou, B. Dong, and W. Li, Phase-field-based lbm analysis of khi and rti in wide ranges of density ratio, viscosity ratio, and reynolds number, *Int. J. Aerospace Eng.* **2020**, 8885226 (2020).
- [28] Y. Zu, A. Li, and H. Wei, Phase-field lattice boltzmann model for interface tracking of a binary fluid system based on the allen-cahn equation, *Phys. Rev. E* **102**, 053307 (2020).
- [29] H. Liang, Y. Li, J. Chen, and J. Xu, Axisymmetric lattice boltzmann model for multiphase flows with large density ratio, *Int. J. Heat. Mass. Transfer* **130**, 1189 (2019).
- [30] P. Sagaut, Toward advanced subgrid models for lattice-boltzmann-based large-eddy simulation: Theoretical formulations, *Comput. Math. Appl.* **59**, 2194 (2010).
- [31] M. Krafczyk, J. Tölke, and L.-S. Luo, Large-eddy simulations with a multiple-relaxation-time lbe model, *Int. J. Mod. Phys. B* **17**, 33 (2003).
- [32] S. Chen, J. Tölke, and M. Krafczyk, Simple lattice boltzmann subgrid-scale model for convectional flows with high rayleigh numbers within an enclosed circular annular cavity, *Phys. Rev. E* **80**, 026702 (2009).
- [33] S. Jafari and M. Rahnama, Shear-improved smagorinsky modeling of turbulent channel flow using generalized lattice boltzmann equation, *Int. J. Numer. Methods Fluids* **67**, 700 (2011).
- [34] M. Stiebler, M. Krafczyk, S. Freudiger, and M. Geier, Lattice boltzmann large eddy simulation of subcritical flows around a sphere on non-uniform grids, *Comput. Math. Appl.* **61**, 3475 (2011).
- [35] O. Malaspina and P. Sagaut, Consistent subgrid scale modelling for lattice boltzmann methods, *J. Fluid Mech.* **700**, 514 (2012).
- [36] A. Banari, C. Janßen, S. T. Grilli, and M. Krafczyk, Efficient gpgpu implementation of a lattice boltzmann model for multiphase flows with high density ratios, *Comput. Fluids* **93**, 1 (2014).
- [37] A. Banari, C. F. Janßen, and S. T. Grilli, An efficient lattice boltzmann multiphase model for 3d flows with large density ratios at high reynolds numbers, *Comput. Math. Appl.* **68**, 1819 (2014).
- [38] H. Amirshaghghi, M. H. Rahimian, H. Safari, and M. Krafczyk, Large eddy simulation of liquid sheet breakup using a two-phase lattice boltzmann method, *Comput. Fluids* **160**, 93 (2018).
- [39] Y. Sun and C. Beckermann, Sharp interface tracking using the phase-field equation, *J. Comput. Phys.* **220**, 626 (2007).
- [40] P.-H. Chiu and Y.-T. Lin, A conservative phase field method for solving incompressible two-phase flows, *J. Comput. Phys.* **230**, 185 (2011).
- [41] H. Liang, H. Liu, Z. Chai, and B. Shi, Lattice boltzmann method for contact-line motion of binary fluids with high density ratio, *Phys. Rev. E* **99**, 063306 (2019).
- [42] H. Yoshida and M. Nagaoka, Multiple-relaxation-time lattice boltzmann model for the convection and anisotropic diffusion equation, *J. Comput. Phys.* **229**, 7774 (2010).
- [43] A. Rahimi, A. Kasaeipoor, A. Amiri, M. H. Doranehgard, E. H. Malekshah, and L. Kolsi, Lattice boltzmann method based on dual-mrt model for three-dimensional natural convection and entropy generation in cuo–water nanofluid filled cuboid enclosure included with discrete active walls, *Comput. Math. Appl.* **75**, 1795 (2018).
- [44] S. O. Unverdi and G. Tryggvason, A front-tracking method for viscous, incompressible, multi-fluid flows, *J. Comput. Phys.* **100**, 25 (1992).
- [45] J. Kim, A continuous surface tension force formulation for diffuse-interface models, *J. Comput. Phys.* **204**, 784 (2005).
- [46] D. d’Humières, Multiple–relaxation–time lattice boltzmann models in three dimensions, *Philos. Trans. R. Soc. London, Ser. A* **360**, 437 (2002).
- [47] Q. Lou, Z. Guo, and B. Shi, Effects of force discretization on mass conservation in lattice boltzmann equation for two-phase flows, *Europhys. Lett.* **99**, 64005 (2012).
- [48] S. Hou, J. Sterling, S. Chen, and G. D. Doolen, A lattice boltzmann subgrid model for high reynolds number flows, *Fields Inst. Comm.* **6**, 151 (1996).
- [49] J. Chesnel, T. Menard, J. Reveillon, and F.-X. Demoulin, Sub-grid analysis of liquid jet atomization, *Atomization Spray*, **21**, 41 (2011).
- [50] J. Smagorinsky, General circulation experiments with the primitive equations: I. the basic experiment, *Mon. Weather Rev.* **91**, 99 (1963).
- [51] Y. Ba, H. Liu, Q. Li, Q. Kang, and J. Sun, Multiple-relaxation-time color-gradient lattice boltzmann model for simulating two-phase flows with high density ratio, *Phys. Rev. E* **94**, 023310 (2016).
- [52] P. J. Love, P. V. Coveney, and B. M. Boghosian, Three-dimensional hydrodynamic lattice-gas simulations of domain growth and self-assembly in binary immiscible and ternary amphiphilic fluids, *Phys. Rev. E* **64**, 021503 (2001).
- [53] J. Chin and P. V. Coveney, Lattice boltzmann study of spinodal decomposition in two dimensions, *Phys. Rev. E* **66**, 016303 (2002).
- [54] N. González-Segredo, M. Nekovee, and P. V. Coveney, Three-dimensional lattice-boltzmann simulations of critical spinodal



- decomposition in binary immiscible fluids, *Phys. Rev. E* **67**, 046304 (2003).
- [55] H. Chen and A. Chakrabarti, Surface-directed spinodal decomposition: Hydrodynamic effects, *Phys. Rev. E* **55**, 5680 (1997).
- [56] M. E. Cates, V. M. Kendon, P. Bladon, and J.-C. Desplat, Introductory lecture: Inertia, coarsening and fluid motion in binary mixtures, *Faraday Discuss.* **112**, 1 (1999).
- [57] S. Leclaire, N. Pellerin, M. Reggio, and J.-Y. Trépanier, Multiphase flow modeling of spinodal decomposition based on the cascaded lattice boltzmann method, *Physica A (Amsterdam, Neth.)* **406**, 307 (2014).
- [58] K. Yang and Z. Guo, Lattice boltzmann study of wettability alteration in the displacement of nanoparticle-filled binary fluids, *Comput. Fluids* **124**, 157 (2016).
- [59] T. Ohta, D. Jasnow, and K. Kawasaki, Universal Scaling in the Motion of Random Interfaces, *Phys. Rev. Lett.* **49**, 1223 (1982).
- [60] R. Verberg, J. M. Yeomans, and A. C. Balazs, Modeling the flow of fluid/particle mixtures in microchannels: Encapsulating nanoparticles within monodisperse droplets, *J. Chem. Phys.* **123**, 224706 (2005).
- [61] X. He, R. Zhang, S. Chen, and G. D. Doolen, On the three-dimensional rayleigh–taylor instability, *Phys. Fluids* **11**, 1143 (1999).
- [62] Y. Wang, C. Shu, and L. Yang, An improved multiphase lattice boltzmann flux solver for three-dimensional flows with large density ratio and high reynolds number, *J. Comput. Phys.* **302**, 41 (2015).
- [63] H. Liang, B. Shi, and Z. Chai, An efficient phase-field-based multiple-relaxation-time lattice boltzmann model for three-dimensional multiphase flows, *Comput. Math. Appl.* **73**, 1524 (2017).
- [64] M. Rieber and A. Frohn, A numerical study on the mechanism of splashing, *Int. J. Heat Fluid Flow* **20**, 455 (1999).
- [65] W. v. Ohnesorge, Die bildung von tropfen an düsen und die auflösung flüssiger strahlen, *J. Appl. Math. Mech.* **16**, 355 (1936).
- [66] L. Li, X. Jia, and Y. Liu, Modified outlet boundary condition schemes for large density ratio lattice boltzmann models, *J. Heat Transfer* **139**, 052003 (2017).
- [67] J. Shinjo and A. Umemura, Simulation of liquid jet primary breakup: Dynamics of ligament and droplet formation, *Int. J. Multiphas. Flow* **36**, 513 (2010).
- [68] S. Saito, Y. Abe, and K. Koyama, Lattice boltzmann modeling and simulation of liquid jet breakup, *Phys. Rev. E* **96**, 013317 (2017).
- [69] S. Saito, Y. Abe, and K. Koyama, Flow transition criteria of a liquid jet into a liquid pool, *Nucl. Eng. Des.* **315**, 128 (2017).
- [70] N. I. Kolev, *Multiphase Flow Dynamics* (Springer-Verlag, Berlin, Heidelberg, 2005), Vol. 1.